

**Finite Element Method Modeling of Optoconductance in
Semiconductor-Metal Hybrid Devices**

by

Alexi M. Girgis

A Thesis

Submitted to the Faculty

of the

WORCESTER POLYTECHNIC INSTITUTE


In partial fulfillment of the requirements for the

Degree of Doctor of Philosophy

in

Physics

by

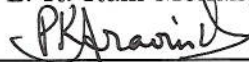


November 2010

APPROVED:



Professor L. R. Ram-Mohan, Ph.d Advisor



Professor P.K. Aravind, Committee Member



Professor John Sullivan, Committee Member



Professor Germano Iannacchione, Department Head

Abstract

A numerical description of the extraordinary optoconductance (EOC) effect is presented using two separate models. Extraordinary optoconductance is part of a general class of EXX geometric effects involving the external perturbation of the properties of a 2D electron gas in a macroscopic semiconductor or metal-semiconductor hybrid structure. The addition of metallic inclusions, has been shown to increase the sensitivity of devices relying on EXX effects. Following the discovery of the first EXX effect, extraordinary magneto-resistance (EMR), an optical equivalent was suggested. Unlike EMR, where the external perturbation is an applied magnetic field, EOC results from the modification of the local charge density in the semiconductor by a focused laser.

The first model assumes Gaussian charge densities for the photo-generated electron-hole pairs while the second model directly solves the semiconductor drift-diffusion equations using the finite element method (FEM). Results from both models are shown to agree with experimental EOC data, both as a function of the laser spot position and temperature. The FEM model has the ability to describe EOC in more complex geometries making it useful in designing EOC devices geared for particular applications.

Acknowledgements

I wish to thank my advisor, Professor L.R. Ram-Mohan for providing me with unique opportunities spanning several years. During this time I had the privilege of working with groups at a number of institutions on a wide variety of problems.

I thank my collaborators on this work, Dr. Stuart Solin, Dr. Kris Weiland, and Yun Wang from the Center for Materials Innovation at Washington University in St. Louis. They have proven to be a valuable experimental connection for several years.

Dr. Keon-Ho Yoo of Kyung Hee University in Seoul, South Korea provided useful discussions and insight during his visits to WPI. Additionally, I thank him, as well as Dr. John Albrecht of Air Force Research Laboratory, for support in obtaining my fellowship.

I wish to thank the National Science Foundation for past support and the ASEE SMART Fellowship for recent support of my doctoral work.

I wish to thank the Tata Institute of Fundamental Research in Mumbai for their hospitality during my 2008 visit. In particular, Dr. K.L. Narasimhan, for his work in organizing the school on the finite element method which prompted the visit.

I am grateful to the committee members, Professor P.K. Aravind of the Department of Physics and Professor John Sullivan of the Mechanical Engineering Department for arranging the defense.

I thank the Department of Physics at Worcester Polytechnic Institute for supporting me over the years. In particular for providing teaching opportunities when necessary. I wish to thank our department head Professor Germano Iannacchione for his guidance.

Contents

1	Introduction	1
2	Gaussian Charge Model	4
3	Drift-Diffusion Model	9
3.1	Finite Element Method	12
3.1.1	Drift-Diffusion Equation	12
3.1.2	Poisson Equation	13
4	Results	16
4.1	Dependence of EOC on Laser Spot Position	16
4.2	EOC Bias Current Dependence	18
4.3	EOC Laser Power Dependence	19
4.4	EOC Temperature Dependence	20
A	Experimental Procedure and Sample Characterization	23
A.1	Experimental Setup	23
A.2	Sample Characterization	24
A.3	Experimental Procedure	25

List of Figures

1.1	A diagram illustrating the four-probe resistance measurement.	2
2.1	The EOC device geometry with a metallic shunt. A constant bias current I_{14} is supplied through leads 1 and 4 while the voltage difference between leads 2 and 3 is measured. The laser illuminates a focal region of radius R at a position \mathbf{r}_ℓ	5
2.2	The electron and hole number densities (solid curves) and the net charge density (dashed curve) as a function of the coordinate s . The diffusion lengths for electrons and holes are indicated with dotted lines.	7
2.3	The measured (points) and calculated (curves) voltage V_{23} as a function of the x -coordinate of the laser spot x_ℓ with fixed values of $y_\ell = 300 \mu\text{m}$ and $y_\ell = 800 \mu\text{m}$	8
3.1	The excess hole density \bar{p} in a) the bare device and b) the MSH device at the laser spot position $(x_\ell, y_\ell) = (4, 0.7)$ mm.	13
3.2	The potential due to the excess hole density \bar{p} in a) the bare device and b) the MSH device at the laser spot position $(x_\ell, y_\ell) = (4, 0.7)$ mm.	15

4.1	The measured voltage V_{23} as the laser spot is moved in the x-direction for $y_\ell = 0.2$ mm and $y_\ell = 0.7$ mm for the bare sample a) and the MSH sample b). The curves represent theoretical calculations and the points represent experimental measurements taken at 15 K with a power density of 6.3×10^4 W cm ⁻²	17
4.2	The measured voltage V_{23} as the laser spot is moved in the y-direction for $x = 3.3$ mm for the bare sample and MSH sample. The curves represent theoretical calculations and the points represent experimental measurements taken at 15 K with a power density of 6.3×10^4 W cm ⁻²	18
4.3	The measured voltage V_{23} versus laser power at spot position $\mathbf{r}_\ell = (3.3, 0)$ mm for the bare sample (boxes) and the MSH sample (circles) at room temperature. The lines represent the calculated value of V_{23} versus the quantity αG_0 , where α is a proportionality constant which differs for the bare and MSH devices (see Table 4.1).	19
4.4	The temperature dependence of the EOC. The measurements were acquired at spot positions $x_\ell = 3.3$ mm with various values of y_ℓ (points). The curves are the corresponding finite element method calculations. Experimental measurements were taken with a power density of 6.3×10^4 W cm ⁻²	21
A.1	The experimental setup used to characterize the EOC devices.	24

List of Tables

2.1	Parameters for n-type GaAs at $T = 300$ K with the minority carrier lifetime assumed to be $\tau_r = 0.5$ ns.	6
4.1	The proportionality coefficients α relating the laser power density P to the generation rate G_0	20

Chapter 1

Introduction

The discovery of extraordinary magneto-resistance (EMR) by Solin *et al.*[1, 2] led to similar metal-semiconductor hybrid (MSH) devices based on modification of the transport properties by an external perturbation. The distinguishing feature of such devices is the use of geometry to enhance sensitivity. In the case of EMR, an applied magnetic field alters the current distribution in a MSH device, effectively changing the device resistance. The magneto-resistance is the percent change in resistance due to the applied magnetic field

$$MR = \frac{R(B) - R(B = 0)}{R(B = 0)} \times 100. \quad (1.1)$$

The resistance is measured using a four-probe resistance measurement as illustrated in Figure 1.1. The four-probe device resistance is then $R = \frac{V_{23}}{I_{14}}$ such that the MR can be written in terms of the measured voltage only. The addition of a metallic shunt along the top side of the semiconductor, making the device a MSH, drastically improves sensitivity with EMR reaching 500% in some cases[3]. This simple addition makes EMR devices more sensitive than giant magneto-resistance sensors used in some hard drive read heads. A finite element method (FEM) description of EMR in

the van der Pauw geometry, was developed by Moussa *et al.*[4] and subsequently used to describe the response of such EMR devices to a magnetic bit[5], similar to those found in magnetic storage media.

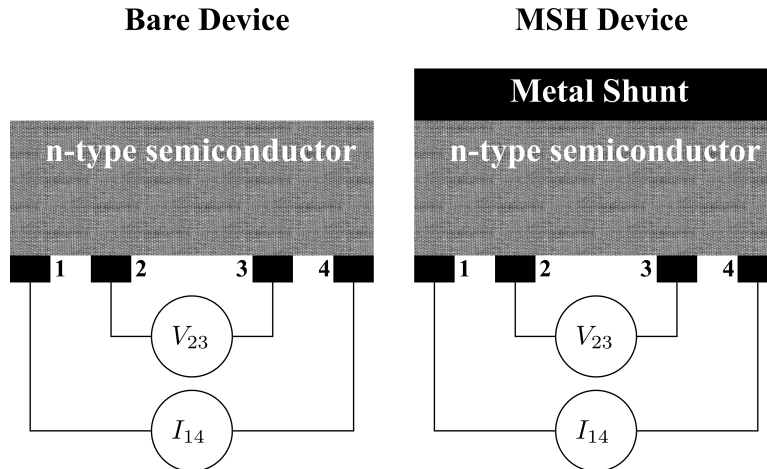


Figure 1.1: A diagram illustrating the four-probe resistance measurement.

Extraordinary optoconductance (EOC) is a related effect in which the external perturbation is a focused laser beam, rather than a magnetic field. Although the geometry and electrical measurements of EOC are similar to that of EMR, the mechanism by which the external perturbation affects the device properties is quite different. Extraordinary optoconductance relies on the Dember effect[6], which is a direct result of the disparity between the electron and hole mobilities in the semiconductor. Illumination from the laser creates electron-hole pairs and both types of carriers diffuse away from the region illuminated by the laser spot. In certain semiconductors such as GaAs, the electron mobility is many times larger than that of holes[7], causing the electrons to diffuse at a faster rate. The steady state electron density is delocalized as compared to the hole density. The resulting net charge density from photo-generated carriers is responsible for the effective change in the device resistance and correspondingly the measured voltage. The addition of a

metallic shunt, as in EMR, enhances the change in resistance due to the external perturbation in EOC. The extraordinary optoconductance is the percent change in resistance due to the addition of the shunt,

$$EOC = \frac{R_{\text{shunt}} - R_{\text{w/o shunt}}}{R_{\text{w/o shunt}}} \times 100. \quad (1.2)$$

The definition above makes EOC somewhat different than EMR. The EOC is a figure of merit indicating the effectiveness of adding the metallic shunt, whereas the EMR describes the change in resistance due to the strength of the external perturbation.

The following chapters detail two models for optoconductance. Chapter 2 describes a phenomenological model which assumes the photogenerated electron and hole charge densities to be Gaussian functions. Chapter 3 describes the finite element method (FEM) model which directly solves the drift-diffusion equation. The results of the drift-diffusion model are presented in Chapter 4.

Chapter 2

Gaussian Charge Model

Developing a theoretical model of EOC based devices requires consideration of the physical processes involved. The laser illuminates a circular region in the semiconductor, thereby creating a region of electron-hole pair generation. The electrons and holes diffuse away from the laser spot. As noted by Dember[6], the electron mobility is much higher than that of holes in GaAs. As a result, the electrons diffuse at a faster rate leaving behind an excess positive charge density. The excess charge in the focal region alters the device resistance depending on the laser spot position, temperature, excitation wavelength, and power density. Most importantly, the measured voltage depends on the proximity to the metallic shunt that enhances the removal of the photogenerated carriers, and thus quantitatively affects the excess charge in the device. Figure 2.1 shows an EOC metal-semiconductor device along with the coordinates used in the modeling. The focal region of the laser is a circle of radius R centered at a position \mathbf{r}_ℓ . The contacts, labeled 1-4 in Figure 2.1, are at positions x_i , although only x_2 and x_3 are shown. A constant bias current is supplied through leads 1 and 4 while the voltage difference between leads 2 and 3 is measured.

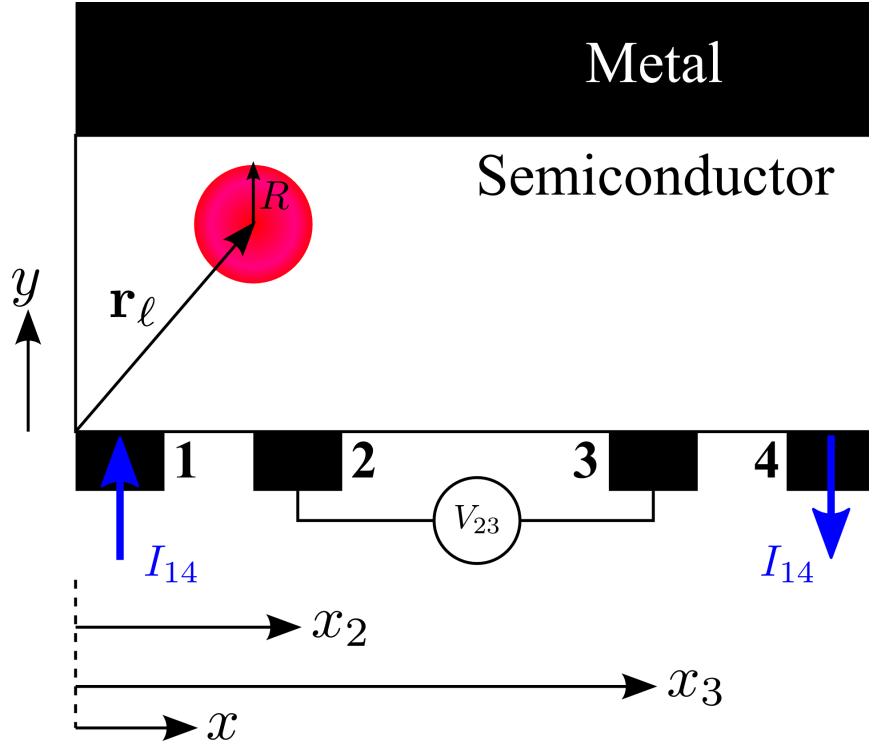


Figure 2.1: The EOC device geometry with a metallic shunt. A constant bias current I_{14} is supplied through leads 1 and 4 while the voltage difference between leads 2 and 3 is measured. The laser illuminates a focal region of radius R at a position \mathbf{r}_ℓ .

As mentioned previously, EOC is the result of the net charge due to the difference in diffusion coefficients of electrons and holes. A natural choice for diffusive systems is a Gaussian charge density as it is the fundamental solution of the free space diffusion equation. The charge densities for electrons and holes are written as

$$\rho_n(s) = \frac{Q_n}{\pi L_n^2} \exp(-s^2/L_n^2), \quad (2.1)$$

$$\rho_p(s) = \frac{Q_p}{\pi L_p^2} \exp(-s^2/L_p^2), \quad (2.2)$$

where the coordinate s is relative to the center of the laser spot. The charge densities ρ_n and ρ_p are normalized to Q_n and Q_p respectively, both of which are adjustable parameters in the calculation. The quantities L_n and L_p are the diffusion lengths

for electrons and holes. The diffusion length is the average length over which a carrier travels before recombination and is related to the diffusion coefficient and the minority carrier recombination time by

$$L_{(n,p)} = \sqrt{D_{(n,p)}\tau_r}. \quad (2.3)$$

The minority carrier lifetime for n-type GaAs was taken to be $\tau_r = 0.5$ ns in our calculations leading to the following material parameters at room temperature. The

Parameter (@ $T = 300$ K)	Electrons	Holes
Mobility ($\text{cm}^2 \text{V}^{-1} \text{s}^{-1}$)	2100	150
Diffusion Coefficient ($\text{cm}^2 \text{s}^{-1}$)	54.3	3.9
Diffusion Length (μm)	1.65	0.44

Table 2.1: Parameters for n-type GaAs at $T = 300$ K with the minority carrier lifetime assumed to be $\tau_r = 0.5$ ns.

potential difference $V_{23}^{(n,p)}$ due to the charge density $\rho_{(n,p)}$ is obtained by integration over the Green's function evaluated at the two voltage probe locations \mathbf{r}_2 and \mathbf{r}_3 ,

$$V_{23}^{(n,p)} = \frac{1}{4\pi\epsilon} \iint d^2s \rho_{(n,p)}(s) \left[\frac{1}{|\mathbf{r}_2 - (\mathbf{r}_\ell + \mathbf{s})|} - \frac{1}{|\mathbf{r}_3 - (\mathbf{r}_\ell + \mathbf{s})|} \right]. \quad (2.4)$$

The integration in Eq. 2.4 was performed separately for the electron and hole charge densities because of the differing length scales. Figure 2.2 shows the electron and hole number densities according to the parameters in Table 2.1. Figure 2.3 shows the calculated voltage difference V_{23} versus the laser spot x -coordinate x_ℓ for $y_\ell = 300 \mu\text{m}$ and $y_\ell = 800 \mu\text{m}$ as compared to the corresponding experimental data. The experimental data was obtained at $y_\ell = 0 \mu\text{m}$ and $y_\ell = 500 \mu\text{m}$ rather than $y_\ell = 300 \mu\text{m}$ and $y_\ell = 800 \mu\text{m}$ due to difficulties in establishing the $y_\ell = 0$ position.

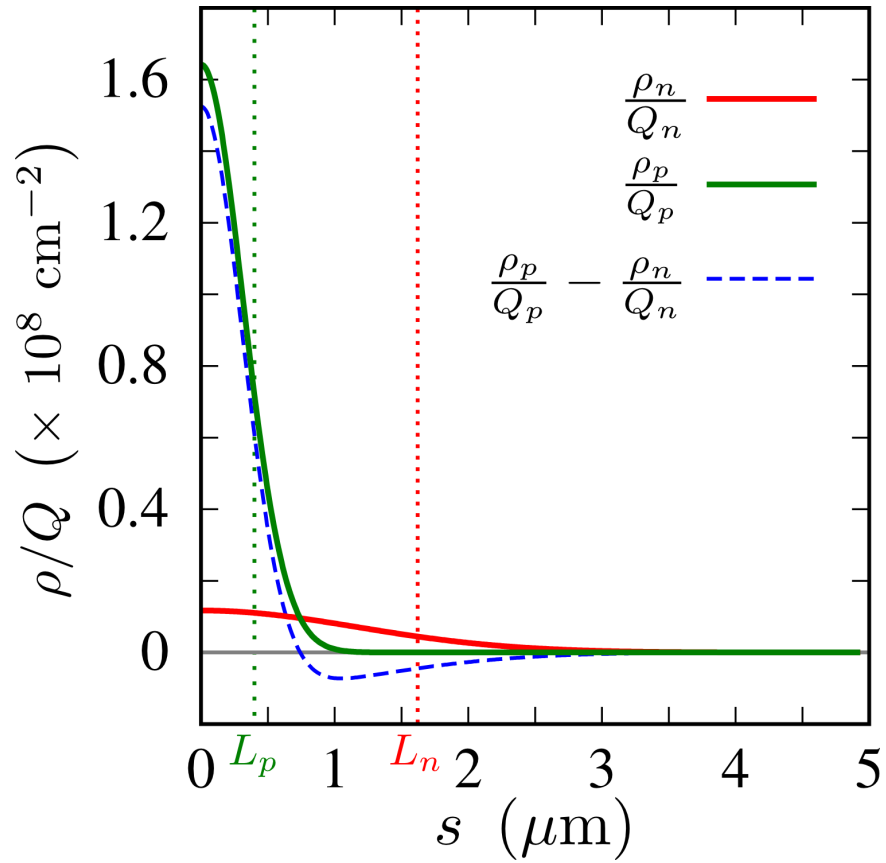


Figure 2.2: The electron and hole number densities (solid curves) and the net charge density (dashed curve) as a function of the coordinate s . The diffusion lengths for electrons and holes are indicated with dotted lines.

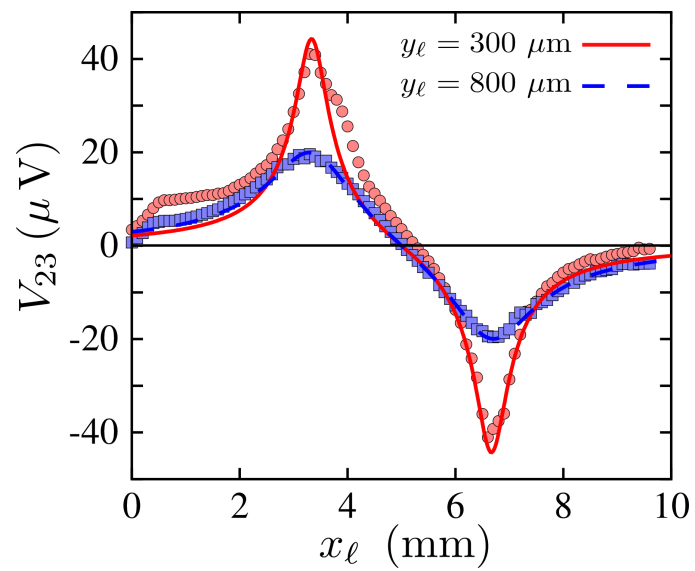


Figure 2.3: The measured (points) and calculated (curves) voltage V_{23} as a function of the x -coordinate of the laser spot x_{ℓ} with fixed values of $y_{\ell} = 300 \mu\text{m}$ and $y_{\ell} = 800 \mu\text{m}$.

Chapter 3

Drift-Diffusion Model

Following the arguments of McKelvey[8] and Chuang[9] the current in a semiconductor generally has both resistive and diffusive terms,

$$\mathbf{J}_n = q [\mu_n n \mathbf{E} + D_n \nabla n], \quad (3.1)$$

$$\mathbf{J}_p = q [\mu_p p \mathbf{E} - D_p \nabla p], \quad (3.2)$$

where $n(x, y)$ and $p(x, y)$ are the spatially dependent electron and hole number densities and μ_n and μ_p are their respective mobilities. The quantity $q = |e|$ is the magnitude of the electron charge. The quantities D_n and D_p are the temperature dependent diffusion coefficients defined by the Einstein relations

$$D_n = \frac{\mu_n k_b T}{q}, \quad (3.3)$$

$$D_p = \frac{\mu_p k_b T}{q}. \quad (3.4)$$

The effects of electron-hole generation and recombination are taken into account in the continuity equations,

$$\frac{1}{q}\nabla \cdot \mathbf{J}_n + G(x, y) - R_n(x, y) = \frac{\partial n}{\partial t}, \quad (3.5)$$

$$-\frac{1}{q}\nabla \cdot \mathbf{J}_p + G(x, y) - R_p(x, y) = \frac{\partial p}{\partial t}, \quad (3.6)$$

where $G(x, y)$ is the spatially dependent generation rate per unit volume, and $R_n(x, y)$ and $R_p(x, y)$ are the recombination rates for electrons and holes. Using Eqs. 3.1 and 3.2 in the continuity equations gives the steady state semiconductor drift-diffusion equations,

$$\nabla \cdot [D_n \nabla n + \mu_n n \mathbf{E}] + G(x, y) - R_n(x, y) = 0, \quad (3.7)$$

$$\nabla \cdot [D_p \nabla p - \mu_p p \mathbf{E}] + G(x, y) - R_p(x, y) = 0. \quad (3.8)$$

The carrier number densities can be written as $n = n_0 + \bar{n}$ and $p = p_0 + \bar{p}$. In the case at hand, the semiconductor is n-type and degenerately doped with $p_0 \approx 0$, and the equilibrium electron number density n_0 is much larger than the excess electron density \bar{n} . As noted above, in GaAs, the electron mobility is several times larger than that of holes. As a result, the excess electrons diffuse away rapidly from the laser spot and therefore can be viewed as a small increase in the large equilibrium electron density. Moreover, since $p_0 \approx 0$, the total hole number density is simply equal to the excess hole number density \bar{p} . From these assumptions follows an approximate charge neutrality, in which the electron number density remains close to n_0 . As a result of these assumptions, it is suitable to solve only the hole drift-diffusion

equation,

$$\nabla \cdot [D_p \nabla \bar{p} - \mu_p \bar{p} \mathbf{E}] + G(x, y) - R_p(x, y) = 0, \quad (3.9)$$

where the quantity \mathbf{E} is the local electric field. The recombination rate for holes is assumed to be proportional to the hole number density, $R_p(x, y) = \frac{\bar{p}}{\tau_r}$, where τ_r is the minority carrier recombination lifetime. The generation rate $G(x, y)$ is assumed to be a Gaussian, with the average radius being equal to the spot radius R of the illuminating laser

$$G(s) = G_0 \exp \left[\frac{\pi}{4} \left(\frac{s}{R} \right)^2 \right]. \quad (3.10)$$

Here G_0 is the generation rate per unit volume at the laser spot center, and the value of the coordinate s is relative to the spot center position \mathbf{r}_ℓ . The drift diffusion equation for holes is now given by,

$$\nabla \cdot [D_p \nabla \bar{p} - \mu_p \bar{p} \mathbf{E}] + G_0 \exp \left[\frac{\pi}{4} \left(\frac{s}{R} \right)^2 \right] - \frac{\bar{p}}{\tau} = 0. \quad (3.11)$$

In order to solve Eq. 3.11, we set $\bar{p} = 0$ on the current ports 1 and 4, and also in the metallic shunt region. The first boundary condition asserts that any net hole distribution on the current ports will recombine with the electrons in the indium leads. The second boundary condition is due to the fact that the shunt is metallic and therefore any hole states will be short lived (ie. $\tau_r = 0$ in the metal). These boundary conditions are straightforward to implement within the framework of the FEM.

3.1 Finite Element Method

3.1.1 Drift-Diffusion Equation

The solution of Eq. 3.11 is obtained using the Galerkin Finite Element Method with the weight functions ϕ being the same functions as the interpolation polynomials used to represent the number density in each finite element. Multiplying Eq. 3.11 by the Galerkin weight function and integrating gives,

$$\iint \phi \nabla \cdot [D_p \nabla \bar{p} - \mu_p \bar{p} \mathbf{E}] dA - \frac{1}{\tau} \iint \phi \bar{p} dA = \iint \phi G_0 \exp \left[\frac{\pi}{4} \left(\frac{r}{r_\ell} \right)^2 \right] dA. \quad (3.12)$$

The first integral in the above equation is integrated by parts to yield

$$\begin{aligned} - \iint \nabla \phi \cdot [D_p \nabla \bar{p} - \mu_p \bar{p} \mathbf{E}] dA + \oint \phi D_p \nabla \bar{p} \cdot \hat{n} dl - \frac{1}{\tau} \iint \phi \bar{p} dA & \quad (3.13) \\ = \iint \phi G_0 \exp \left[\frac{\pi}{4} \left(\frac{r}{r_\ell} \right)^2 \right] dA. & \end{aligned}$$

The surface integral in the above equation represents a flux of holes through the external boundary and is included only at the current ports. The hole current at the current ports can be calculated using

$$I_{port} = qd \int_{port} D_p \nabla \bar{p} \cdot \hat{n} dl, \quad (3.14)$$

where d is the sample thickness. These diffusive currents must be included in determining the net current flowing through the device. The applied voltage necessary for maintaining the net current at its given value is calculated by determining the effective device resistance including all carriers. This voltage is applied as the boundary condition for the Poisson equation. Figure 3.1 shows the excess hole density for the

bare and MSH devices at the laser spot position $(x_\ell, y_\ell) = (4, 0.7)$ mm. The excess

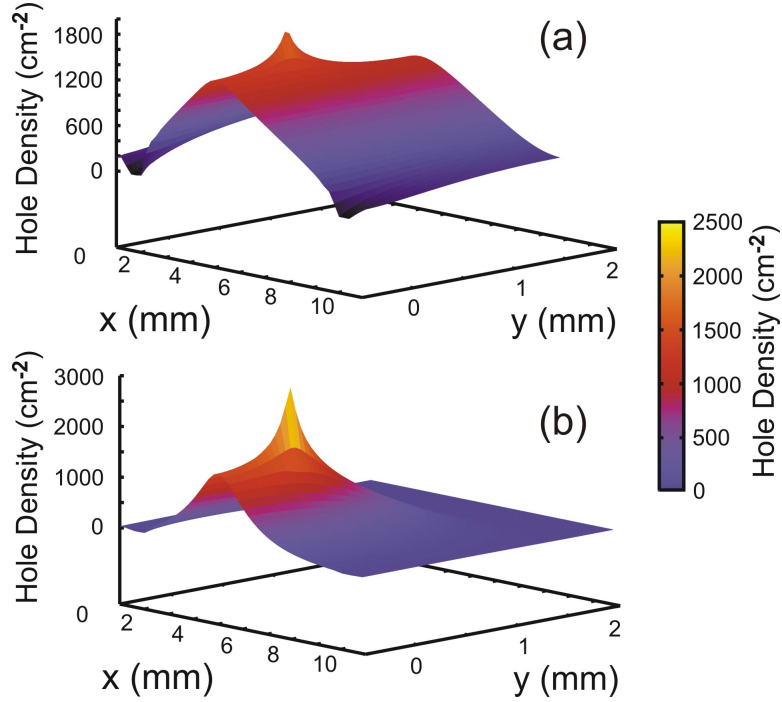


Figure 3.1: The excess hole density \bar{p} in a) the bare device and b) the MSH device at the laser spot position $(x_\ell, y_\ell) = (4, 0.7)$ mm.

hole density is larger in the MSH device due to the effectiveness of the shunt at removing excess electrons.

3.1.2 Poisson Equation

The Poisson equation for the potential due to the excess hole density is

$$\nabla \cdot [\epsilon \nabla V] = -q\bar{p}, \quad (3.15)$$

where ϵ is the material permittivity. Equation 3.15 is solved using the Galerkin FEM for the electrostatic potential due to the excess hole density with the boundary conditions that the applied voltage mentioned above is applied across the current

ports 1 and 4, while the voltages at ports 2 and 3 (see Figure 2.1) are determined by the solution. The steps for calculating the potential due to the photo-generated carriers are outlined below for one laser spot position:

1. Solve the drift-diffusion equation (Eq. 3.11) for \bar{p} .
2. Calculate the current on the input and output current ports using Eq. 3.14 from the solution of Eq. 3.11.
3. Determine the applied voltage V_{14} from the requirement that the net current be equal to the applied bias current.
4. Solve the Poisson equation (Eq. 3.15) with V_{14} applied across ports 1 and 4.
5. Calculate V_{23} using the solution of Eq. 3.15.

Figure 3.2 shows the solution to Eq. 3.15 for laser spot position $(x_\ell, y_\ell) = (4, 0.7)$ mm corresponding to the excess hole densities shown in Fig. 3.1.

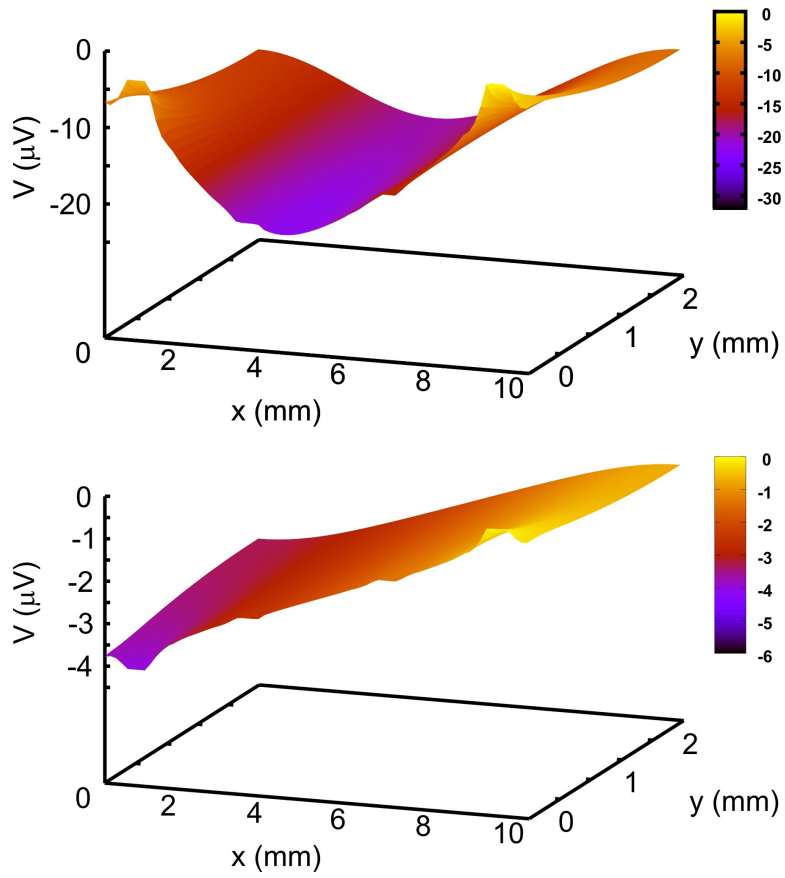


Figure 3.2: The potential due to the excess hole density \bar{p} in a) the bare device and b) the MSH device at the laser spot position $(x_\ell, y_\ell) = (4, 0.7)$ mm.

Chapter 4

Results

4.1 Dependence of EOC on Laser Spot Position

The measured voltage V_{23} and theoretical results (solid lines) are shown in Fig. 4.1 for $y_\ell = 0.2$ mm and $y_\ell = 0.7$ mm as a function of x_ℓ for both the hybrid and bare samples at a temperature of 15 K with a power density of 6.3×10^4 W cm⁻². As x_ℓ increases there is a peak at the location of the V_2 voltage lead. As is evident in Fig. 4.1, the theoretical model reasonably approximates the positional dependence along the x -direction. The generation rate G_0 , which was the only adjustable parameter, was varied such that the measured and calculated voltages coincided at the peak value. The value of the voltage at other x_ℓ positions was determined using the same generation rate which was used to match the peak value. This process of choosing the generation rate was done separately for each value of y_ℓ and for both the bare and shunted sample. Figure 4.2 shows the voltage V_{23} for $x_\ell = 3.3$ mm as a function of y_ℓ , for both the hybrid and bare sample with theory represented by solid and dashed lines. As y_ℓ increases, the measured voltage approaches zero for both the hybrid and bare samples. In addition, with increasing y_ℓ , the charge distributions

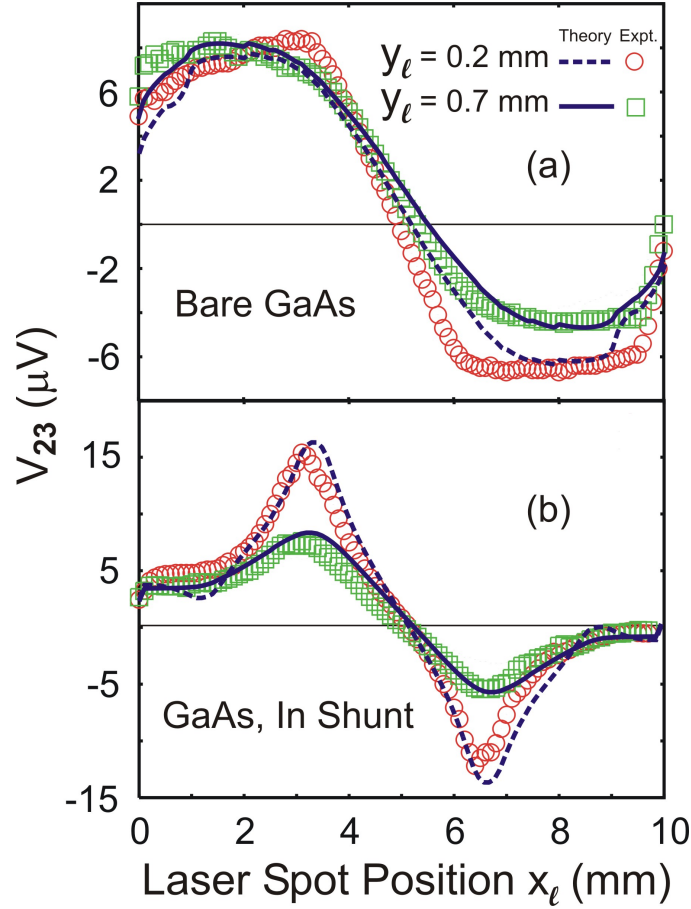


Figure 4.1: The measured voltage V_{23} as the laser spot is moved in the x-direction for $y_\ell = 0.2$ mm and $y_\ell = 0.7$ mm for the bare sample a) and the MSH sample b). The curves represent theoretical calculations and the points represent experimental measurements taken at 15 K with a power density of 6.3×10^4 W cm $^{-2}$.

are further away from the voltage leads and closer to the shunt, thereby lowering the measured voltage. As a result, the voltage in the hybrid sample decreases as the laser spot is moved closer to the shunt. Because of these effects, both V_{23} and the EOC decrease as a function of the y_ℓ , with their peaks being at $y_\ell = 0$. Similar to the x_ℓ dependence, one generation rate for the y_ℓ dependence was chosen such that the theoretical voltages matched the experimental values over the entire range of y_ℓ as closely as possible.

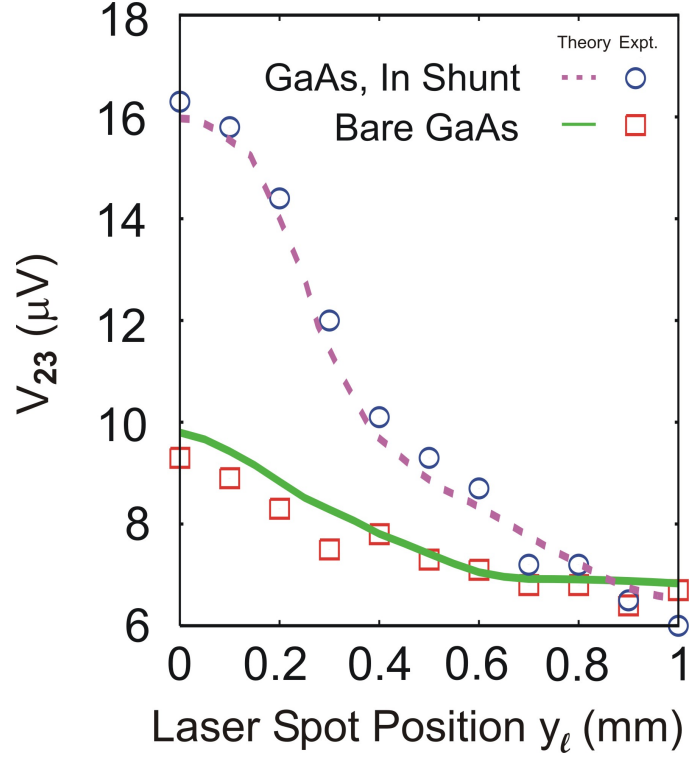


Figure 4.2: The measured voltage V_{23} as the laser spot is moved in the y -direction for $x = 3.3\text{mm}$ for the bare sample and MSH sample. The curves represent theoretical calculations and the points represent experimental measurements taken at 15 K with a power density of $6.3 \times 10^4 \text{ W cm}^{-2}$.

4.2 EOC Bias Current Dependence

The voltages in both the hybrid and bare samples show an offset such that when the laser is not illuminating the sample, the measured voltage V_{23} is nonzero. The voltage offset was seen to be additive to the voltage produced by the excess carriers over the range of bias current I_{14} . In order to calculate the EOC, the offset was removed for both the bare sample and the MSH so that the data reflects the effect of the excess carriers alone. In addition, the voltage offset was found to be proportional to the bias current which suggests that it is associated with the intrinsic sample resistance and not the perturbation that we are interested in.

4.3 EOC Laser Power Dependence

The graph in Fig. 4.3 shows the dependence of V_{23} on the optical power density P at laser spot position $\mathbf{r}_\ell = (3.3, 0)$ mm as measured at $T = 300$ K. The

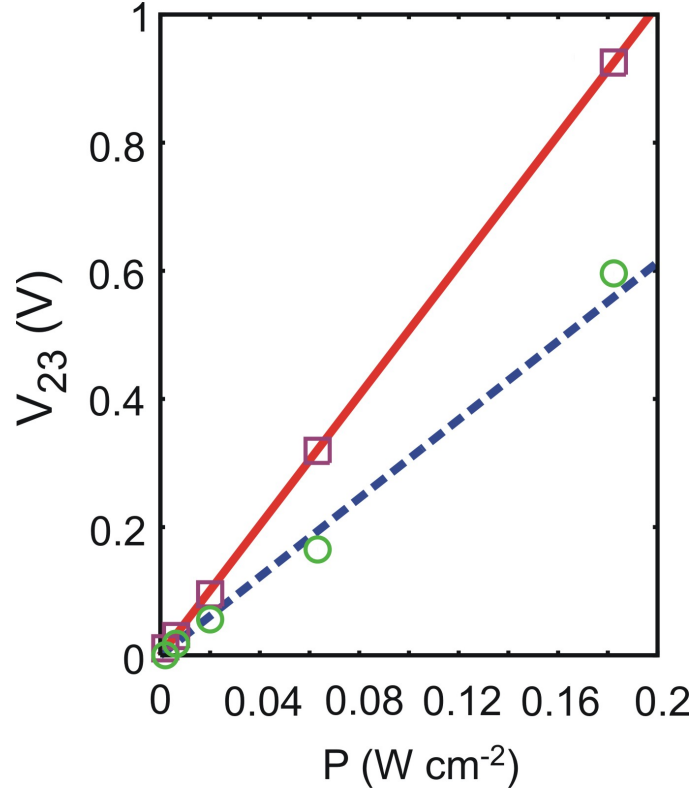


Figure 4.3: The measured voltage V_{23} versus laser power at spot position $\mathbf{r}_\ell = (3.3, 0)$ mm for the bare sample (boxes) and the MSH sample (circles) at room temperature. The lines represent the calculated value of V_{23} versus the quantity αG_0 , where α is a proportionality constant which differs for the bare and MSH devices (see Table 4.1).

theoretical curves indicate that the measured voltage depends linearly on the generation rate. Similarly, the experimental data indicates that the measured voltage depends linearly on the optical power density. These two observations suggest that the generation rate is proportional to the incident power density P , as should be expected in this regime. Table 4.1 lists the coefficients of proportionality used to

match the experimental data in Figure 4.3 for both the bare and MSH sample. The

Device	α ($\text{J}^{-1} \text{cm}^{-1}$)
Bare	4×10^{18}
MSH	1×10^{19}

Table 4.1: The proportionality coefficients α relating the laser power density P to the generation rate G_0 .

difference in α for the two devices arises from geometric contributions which affect the generation and recombination of carriers. Note that the range of power spans approximately two orders of magnitude.

4.4 EOC Temperature Dependence

As reported previously, the EOC reaches a maximum of almost 500 % at 30 K for optimal \mathbf{r}_ℓ values. The EOC displays an inverse relationship to temperature which is discussed below.

The GaAs is degenerately doped with $N_d = 1.25 \times 10^{18} \text{cm}^{-3}$ implying that the equilibrium carrier concentrations n_0 and p_0 change minimally over the temperature range studied[10]. The electron mobility and dielectric constant[7] are also essentially constant over that temperature range. The coefficients in the hole current density (Eq. 3.11) contain both implicit and explicit temperature dependences. According to Lovejoy *et al.*[10] the minority hole mobility in heavily doped GaAs was found to exhibit an inverse temperature dependence such that $\mu_p = \chi T^{-3/2}$. The parameter χ was chosen such that the temperature dependence of the hole mobility corresponds to the data obtained by Lovejoy *et al.*[10]. In Eq. 3.4, there is an explicit linear temperature dependence of the diffusion coefficient. Thus the combined temperature dependence of the diffusion coefficient for holes is proportional

to $T^{-1/2}$. As a result, the effect of the diffusive component decreases with increasing temperature. Figure 4.4 shows the temperature dependence of the EOC for vari-

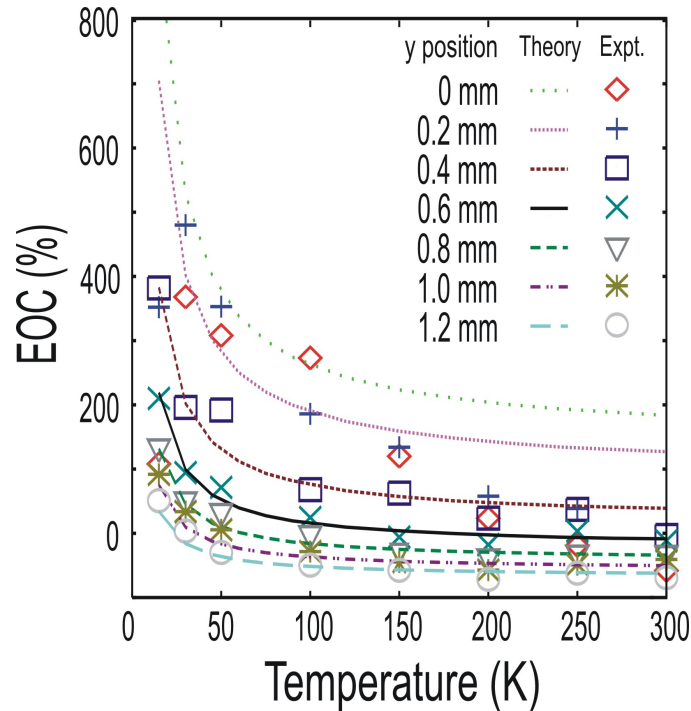


Figure 4.4: The temperature dependence of the EOC. The measurements were acquired at spot positions $x_\ell = 3.3$ mm with various values of y_ℓ (points). The curves are the corresponding finite element method calculations. Experimental measurements were taken with a power density of 6.3×10^4 W cm $^{-2}$.

ous y_ℓ values with a power density of 6.3×10^4 W cm $^{-2}$ at $x_\ell = 3.3$ mm with the points obtained from experiment and the curves calculated from the drift-diffusion model. In the model, the generation rate was held constant for the bare sample, while for the MSH it was scaled to fit the EOC value at one temperature. With G_0 fixed for each y_ℓ in this manner, the temperature dependence of the EOC was then calculated by simply incrementing the temperature. This temperature change, as discussed above, was incorporated directly into the diffusion coefficients as well as the hole mobility. With the exception of $y_\ell = 0$ mm and $y_\ell = 0.2$ mm, the value of G_0 was determined at $T = 15$ K, while at those two values of y_ℓ the $T = 30$ K

values were used.

Appendix A

Experimental Procedure and Sample Characterization

A.1 Experimental Setup

The experimental setup used to measure the EOC is shown in Figure A.1. The bare (shunt-less) sample was illuminated with a Coherent Innova 400 Ar⁺ ion laser operating at 476.5 nm with the beam focused to a 20 μm diameter. The power density was varied from 6.3×10^4 to 5.8×10^6 W cm^{-2} . The samples were mounted in an ARS closed cycle helium cryostat and cooled to temperatures ranging from 10 to 300 K. The cryostat temperature was maintained by a Scientific Instruments 9650 temperature controller. The sample was positioned using a Newport Universal Motion Controller ESP 300 system with three linear DC stepper motors. For optimal spatial resolution, the sample was placed at the focused beam waist, thereby defining the distance from the lens to the sample and the diameter of the laser spot. The bias current was supplied by a Lakeshore 120 current source in the forward and reverse direction from 1 μA to 100 mA across ports 1 and 4, as shown in Fig. 2.1. The

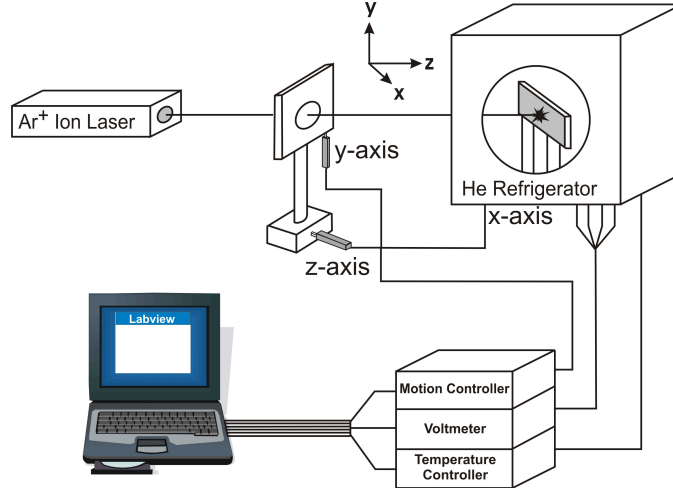


Figure A.1: The experimental setup used to characterize the EOC devices.

voltage was acquired by a Keithley 2182 nanovoltmeter. One channel measured V_{23} and the other channel (not shown) measured the voltage drop across the 1.2Ω resistor in series with the sample. The voltage across the resistor was used to precisely determine the bias current flowing through the device.

A.2 Sample Characterization

Bare samples of dimension $2 \times 10 \times 0.4$ mm were prepared by dicing a 2-inch diameter n-type GaAs wafer grown in the $[001]$ orientation along the 10 mm side. Gallium arsenide was chosen because it is a direct gap (1.424 eV at 300 K) semiconductor and because of optimal absorption in the spectral region of the argon ion laser. The sample was degenerately doped with Si at a concentration $N_d = 1.25 \times 10^{18} \text{ cm}^{-3}$. The electron mobility of the semiconductor was measured to be $2100 \text{ cm}^2 \text{ V}^{-1} \text{ s}^{-1}$. Leads were attached first by metalizing the GaAs, in an inert nitrogen atmosphere, with dots of In (0.2 mm diameter) arranged along the 10 mm side (see Fig. 2). Indium was chosen for metalizing because of its low melting temperature and com-

patibility with GaAs. This setup is similar to the typical four-lead van der Pauw plate setup used elsewhere. This geometry is the conformal equivalent to a van der Pauw disk with an off-centered inclusion. Next, the wires were tinned with In and pressed onto the metalized In dots. Ohmic contacts over the temperature range of interest were confirmed by verifying the linearity of the measured I-V response. These same bare samples were then used to make hybrid samples via the addition of an In shunt. This was achieved by metalizing the bare samples on the side opposite the leads with Indium of dimensions $10 \times 0.5 \times 0.5$ mm. The hybrid sample resistance at room temperature, as measured across ports 1 and 4, decreased by an order of magnitude from that of the bare samples, indicating the effectiveness of the shunt. Ohmic contact at the interface was again verified by the linearity of the I-V response.

A.3 Experimental Procedure

Once the sample position was calibrated, the positional dependence of the voltage V_{23} was studied by moving the laser spot along the x-direction for fixed values of y_ℓ . However, in no case was the interface between the semiconductor and the shunt illuminated by the focused laser beam. Voltages were read every 0.1 mm in the x-direction which provided adequate resolution. Upon reaching the end of the sample, the x-position was returned to zero and the y-position was incremented by 0.1 mm. The program Labview was used to control the sample position and to acquire the data. The experiments were performed under the same conditions for the bare sample and the MSH sample in order to produce consistent results. The position-dependent data acquisition, as outlined above, was repeated for various temperatures, bias currents, and laser power densities.

Bibliography

- [1] S. A. Solin, D. R. Hines, T. Thio, and J. Heremans. Enhanced room-temperature geometric magnetoresistance in inhomogeneous narrow-gap semiconductors. *Science*, 289:1530–1532, 2000.
- [2] S. A. Solin, D. R. Hines, J. S. Tsai, Y. A. Pashkin, S. J. Chung, N. Goel, and M. B. Santos. Nonmagnetic semiconductors as read-head sensors for ultra-high-density magnetic recording. *Appl. Phys. Lett.*, 80:4012, 2002.
- [3] K. A. Wieland, Yun Wang, L. R. Ram-Mohan, and S. A. Solin. Extraordinary optoconductance in metal-semiconductor hybrid structures. *Appl. Phys. Lett.*, 88:52105–52107, 2006.
- [4] J. Moussa, L. R. Ram-Mohan, J. Sullivan, T. Zhou, D. R. Hines, , and S. A. Solin. Finite-element modeling of extraordinary magnetoresistance in thin film semiconductors with metallic inclusions. *Phys. Rev. B*, 64:184410–184417, 2001.
- [5] J. Moussa, L. R. Ram-Mohan, A. C. H. Rowe, , and S. A. Solin. Response of an extraordinary magnetoresistance read head to a magnetic bit. *J. Appl. Phys.*, 94:1110–1114, 2003.
- [6] H. Dember. *Phys. Z.*, 32:554, 1931.
- [7] O. Madelung, editor. *Semiconductors Group IV Elements and III-V Compounds*. Data in Science and Technology. Springer-Verlag, New York, 1991.
- [8] J. P. McKelvey. *Solid State and Semiconductor Physics*. Harper and Row, New York, 1966.
- [9] S. L. Chuang. *Physics of Optoelectronic Devices*. Wiley-Interscience, New York, 1995.
- [10] M. L. Lovejoy, M. R. Melloch, and M. S. Lundstrom. *Appl. Phys. Lett.*, 67:1101, 1995.